Structural tunability and origin of two-level systems in amorphous silicon

H. C. Jacks[*,†] and M. Molina-Ruiz [*,‡]
Physics Department, University of California, Berkeley, California 94720, USA

M. H. Weber
Physics and Astronomy Department, Washington State University, Pullman, Washington 99164, USA

J. J. Maldonis and P. M. Voyles
Materials Science and Engineering Department, University of Wisconsin - Madison, Wisconsin 53706, USA

M. R. Abernathy ,[§] T. H. Metcalf , and X. Liu
Naval Research Laboratory, Washington, DC 20375, USA

F. Hellman
Physics Department, University of California, Berkeley, California 94720, USA
and Lawrence Berkeley National Laboratory, Berkeley, California 94720, USA

Amorphous silicon films prepared by electron-beam evaporation have systematically and substantially greater atomic density for higher thickness, higher growth temperature, and slower deposition rate, reaching the density of crystalline Si when films of thickness greater than ∼300 nm are grown at 425 °C and at <1 Å/s. A combination of spectroscopic techniques provide insight into atomic disorder, local strains, dangling bonds, and nanovoids. Electron diffraction shows that the short-range order of the amorphous silicon is similar at all growth temperatures, but fluctuation electron microscopy shows that films grown above room temperature show a form of medium-range order not previously observed in amorphous silicon. Atomic disorder and local strain obtained from Raman spectroscopy are reduced with increasing growth temperature and show a nonmonotonic dependence on thickness. Dangling bond density decreases with increasing growth temperature and is only mildly dependent on thickness. Positron annihilation Doppler broadening spectroscopy and electron energy loss spectroscopy show that nanovoids, and not density variations within the network, are responsible for reduced atomic density. Specific heat and mechanical loss measurements, which quantify the density of tunneling two-level systems, in combination with the structural data, suggest that two-level systems in amorphous silicon films are associated with nanovoids and their surroundings, which are in essence loosely bonded regions where atoms are less constrained.

I. INTRODUCTION

Amorphous silicon is used in photovoltaic, thin-film transistor, quantum computing, and gravitational-wave detection technologies [1–5], to name a few, since it is much easier to implement than its crystalline counterpart. The performance of amorphous silicon in these technologies is dependent on its properties, which change with the material structure obtained during the preparation process, or by the addition of other elements, such as hydrogen, that improve the electronic properties. Amorphous silicon (*a*-Si) is typically found to be fourfold coordinated, with little variability in bond length, but variability in bond angle and occasional threefold coordination leading to dangling bonds. Fivefold coordinated atoms are found in the liquid phase, but not identified in the solid phase [6,7]. This limited flexibility in the solid phase makes it more controllable than systems with highly variable coordination, e.g., amorphous carbon, or multiatomic materials. Fourfold coordination yields an overconstrained atomic environment, which was postulated by Phillips in 1972 to suppress tunneling two-level systems (TLSs) [8], later confirmed by our work on *a*-Si [9–12].

The suppression of TLSs has been of interest to the glass community because they are the source of energy loss at low temperatures and the origin of anomalous acoustic, thermal, and dielectric properties [13]. The ability to control the TLS density in glasses is crucial in applications for which *a*-Si is a potential material, including phase-resonant qubits

---

*These authors contributed equally to this work.

†Present address: Physics Department, California Polytechnic University, San Luis Obispo, California 93407, USA.

‡Corresponding author: manelmolinaruiz@gmail.com

§Present address: Johns Hopkins University Applied Physics Laboratory, Laurel, Maryland 20723, USA.

[14–16] and coatings for gravitational-wave detection [17,18]. Electron-beam (e-beam) evaporated *a*-Si shows very low TLS density in high-atomic-density films, as opposed to high TLS density found in low-atomic-density films, suggesting that low-density regions are the source of TLSs in e-beam prepared *a*-Si [10–12]. Therefore a careful understanding of the structural differences between these films should lead to a deeper knowledge of the nature of the TLSs. It has been shown that coupled dangling bonds create tunneling states on the surface of hydrogen-terminated crystalline silicon [19], but no correlation between dangling bond density and TLS density has been seen in *a*-Si films [12].

In this paper we present extensive structural characterization of *a*-Si films prepared by e-beam evaporation under ultrahigh-vacuum (UHV) conditions and show how differences in growth temperature, deposition rate, and film thickness affect the growth mechanisms and film properties. We discuss connections between growth parameters and physical properties, as well as between TLS density and structural features. We conclude that nanovoids are the most likely structures responsible for TLSs in e-beam evaporated *a*-Si films.

II. SAMPLE PREPARATION AND CHARACTERIZATION METHODS

Samples were grown by e-beam physical-vapor deposition (PVD) in an UHV chamber with a base pressure of $<5 \times 10^{-9}$ Torr and substrate temperature T_S ranging from 50 to 450 °C, growth rate r_t from 0.5 to 2.5 Å/s, and thickness t from 10 to 750 nm. Samples were grown either onto low-stress amorphous silicon nitride (*a*-SiN$_X$) or onto crystalline silicon with the native oxide layer left intact. A naturally occurring and continuous self-passivating native oxide layer, not thicker than 3 nm [20], was allowed to form on the surface of most *a*-Si films. In some cases, a thin capping layer of Al was used, which forms an excellent passivating layer on exposure to air that protects the film against oxygen and water subsequent to growth.

Structural characterizations, detailed below, span length scales from approximately 0.1 to 10 nm. These techniques provide information on both the network and structural defects of the films, specifically surface topography via atomic force microscopy (AFM), atomic density via Rutherford backscattering spectrometry (RBS) together with profilometry and AFM, short-range order (SRO) and medium-range order (MRO) via electron microscopy, atomic bond angle deviation and local strain via Raman spectroscopy, dangling bond density via electron paramagnetic resonance (EPR), and empty space or nanovoid volume via positron annihilation Doppler broadening spectroscopy (DBS) measurements. RBS was also used to set limits on impurity concentration. Elastic recoil detection analysis (ERDA) was used to quantify the films' water concentration.

With the aim of looking for the depth dependence of atomic density and bond angle deviation and, in particular, to investigate the origin of the differences seen in properties of thin and thick films [10,12], select thick films were etched in order to study structural properties as a function of depth. Films were wet etched to avoid densification or atomic reconstruction via energy transfer, since a dry etch may alter the sample's under-lying atomic structure [21]. To improve thickness control and homogeneity, samples were etched under mild sonication in an isopropanol-saturated 6 M KOH bath at 80 °C for several minutes until specific target thicknesses were reached [22].

A. Atomic force microscopy and substrate curvature

A Digital Instruments AFM Nanoscope Dimension 3100 equipped with Budget Sensors Tap300-G silicon probes with a resonant frequency of 300 kHz and force constant of 40 N/m was used to characterize the samples' surface roughness. The scanned areas are 1×1 μm^2 yielding the root-mean-square (rms) surface roughness R_q and topography of the *a*-Si films, as well as of their substrates.

Substrate curvature measurements were taken using a Tencor FLX-2320 thin-film stress measurement instrument. The stress of *a*-Si films grown on 2-in.-diameter silicon wafers was determined at room temperature using Stoney's equation [23] with no corrections, since the thicknesses ratio between films and substrate ($\sim 10^{-4}$) fulfils the condition of being $\ll 1$ [24].

B. Ion beam analysis and profilometry

The measured atomic density n_{at} of the *a*-Si films is the combined result of profilometry, RBS, and AFM measurements. Profilometry was done using a KLA Tencor ASIQ profilometer, with an error between 0.1 and 4% for the thicker and thinner films, respectively. Ion beam analysis was performed by RBS and ERDA in an NEC model 5SDH Pelletron tandem accelerator, with α-particle beam energy of 3040 keV. Resonant RBS and ERDA techniques were used to quantify the films' oxygen and hydrogen content (with detection thresholds of 0.5 at. % O and 0.1 at. % H). RBS was also used to quantify the presence of other impurities. SIMNRA analysis software was used to obtain the samples' composition and areal density [25]. The thickness obtained by profilometry was corrected by the roughness measured by AFM in order to accurately determine the films' volume. Although the roughness was small (less than 2 nm even in the roughest films), this correction is very important for thinner films.

C. Electron microscopy

Electron nanodiffraction and electron energy loss spectroscopy (EELS) experiments were performed in a Thermo Fisher Titan scanning transmission electron microscope (STEM) operated at 200 kV. The diffracted electron intensity I as a function of the scattering vector **k** was measured using energy-filtered electron diffraction on a GIF 865ER with a Gatan US1000 CCD camera at a camera length of 840 mm, an energy filtering with a slit width of 20 eV, and a high-coherence, 2-nm-diameter nanoprobe beam with a 0.6 mrad semiconvergence angle. One-hundred 512×512-pixel nanodiffraction patterns were acquired in a 10×10 grid of positions r covering a 25×25 nm^2 area from ten different regions of each sample. The acquisition time for each diffraction pattern was 6 s. Each diffraction pattern was averaged over the azimuthal angle to produce the intensity as a function of the scattering vector magnitude k.

The nanodiffraction data set was used to evaluate short- and medium-range order. SRO was evaluated from $I(k)$, which is

the average of $I(k, r)$ over r. This experiment is the equivalent of a large-area diffraction experiment, but with somewhat worse k resolution due to the convergent probe. MRO was evaluated using the fluctuation electron microscopy (FEM) normalized variance V, defined as

$$V(k) = \frac{\langle I^2(k, r) \rangle}{\langle I(k, r) \rangle^2} - 1, \tag{1}$$

where values within $\langle \rangle$ are averaged over the position r on the sample. V measures the magnitude of spatial fluctuations in the diffracted intensity, which are sensitive to three- and four-body correlation functions [26–29]. In a-Si, MRO spans length scales from approximately the fourth coordination shell (~ 0.8 nm) to just under what is detectable by Bragg diffraction (~ 3 nm) [30]. The position in k of peaks in V is controlled by the interatomic spacing inside nanoscale structural heterogeneities (such as deviations in the distribution of ring sizes; see Ref. [31]), and the magnitude of V is controlled by the size, density, and internal order of the heterogeneities. V was corrected for Poisson noise in I as described in Ref. [27].

EELS was performed at a camera length of 160 mm, a probe convergence angle of 25 mrad, and an EELS collection angle of 52 mrad. The energy dispersion was 0.05 eV/channel, and the energy resolution was 0.8 eV, measured as the full width at half maximum (FWHM) of the zero-loss peak. EELS experiments focused on the bulk plasmon loss, which is sensitive to the volume number density of electrons in the material, n. In the Drude model, the peak plasmon energy $\lambda_0 = \hbar \sqrt{ne^2/\epsilon_0 m}$, where e is the electron charge, m is the electron mass, and ϵ_0 is the permittivity of free space. At constant composition, shifts in n result from shifts in the volume number density of atoms ρ, which has been used, for example, to measure thermal expansion in Al as a means of thermometry [32] and the change in volume of Al on melting [33]. Introducing voids into the sample does not shift λ_0. Instead, it introduces new plasmon modes at different energies associated with the surfaces of the voids. As a result, EELS measurements of λ_0 report the average density of the sample excluding voids, unlike density measurements by RBS or the Archimedes principle, and hence report the average interatomic spacing of the material network.

High-resolution transmission electron microscopy (HRTEM) was performed on a FEI Tecnai-TF30 microscope operated at 300 kV. Images with resolution 2048×2048 pixels were recorded by a Gatan Ultrascan CCD with 1 s exposure time. a-Si films for all transmission electron microscopy (TEM) experiments were ~ 30 nm thick grown at different temperatures on 50×50-μm^2 a-SiN$_X$ membranes 50 nm thick and measured in plan view.

D. Raman spectroscopy

The distribution of atomic bonds, or bond angle deviation, $\Delta\theta$ and the fractional volume change, or local strain, tr(ϵ) were determined by Raman spectroscopy performed using an inVia Renishaw micro-Raman and photoluminescence (PL) system equipped with a 488-nm laser. The laser power was set to ~ 250 μW on a spot with area of ~ 2 μm^2, low enough to prevent degradation or crystallization of the amorphous films. Under these conditions, most of the Raman signal comes

from the top ~ 30 nm of the film due to the laser intensity attenuation.

In a-Si the bond angles have a variability around the tetrahedral angle of 109.5°, the canonical tetrahedral angle in crystalline silicon (c-Si), characterized by $\Delta\theta$. Beeman *et al.* [34] established, and others [35,36] later confirmed, an empirical correlation between $\Delta\theta$ and the FWHM of the a-Si transverse optical (TO) peak, observed at ~ 480 cm^{-1}, which yields $\Delta\theta = ($FWHM $- 15)/6$. tr(ϵ) manifests in c-Si Raman spectra through shifts in the TO peak position ω [37,38]. Strubbe *et al.* [39] demonstrated an empirical relationship between TO peak shifts and local strain in a-Si:H, which is valid for isotropic amorphous vibrational mode frequencies. In vibrational density of states calculations, the TO peak vibrations remain almost unaffected by the presence of H atoms, which indicates that atomic interactions are mostly determined by the nature of Si–Si bonds [39]. Experimental Raman spectra of a-Si and a-Si:H around the TO peak region are quite similar. Therefore the empirical relationship obtained for a-Si:H is also valid for a-Si and establishes $\omega = s\,\text{tr}(\epsilon) + \omega_0$, where $s = -460 \pm 10$ cm^{-1} is a fitting parameter and $\omega_0 \approx 480$ cm^{-1} is the bulk a-Si TO peak position [36].

E. Double-paddle oscillator

Transverse sound velocity v_t measurements of a-Si films were taken at 300 mK using the double-paddle oscillator (DPO) technique described elsewhere [40,41]. The resonant frequency of the second antisymmetric torsional resonance mode (AS2) at ~ 5500 Hz is measured to an accuracy of $< 10^{-5}$ Hz on both the bare and film-laden oscillator. The shear modulus G is measured, and v_t is then calculated as $v_t = \sqrt{G/\rho}$, where ρ is the film mass density.

F. Electron paramagnetic resonance

Electron paramagnetic resonance measurements were used to determine the dangling bond density of the films, using a Bruker ELEXSYS E580 EPR spectrometer with an X-band ER 4123D continuous-wave (CW) resonator at 9.36 GHz. EPR determines the density of dangling bond defects, or unpaired electrons, by measuring the signal strength of the resonant transition between the Zeeman split energy levels of the paramagnetic dangling bond defect. Microwave power (1.5 mW) and magnetic field modulation amplitude (5 G) were adjusted for optimum intensity without line shape distortion. Spectra were measured from 3282 to 3383 G. A bare substrate was used to determine the background contribution, whereas the samples' spin density N_S was determined by double integration of the experimental absorption first-derivative spectra and by comparison to a KCl weak pitch with $N_S = 9.5 \times 10^{12} \pm 5\%$ spins/cm^3 and $g = 2.0028 \pm 0.0002$. These experimental conditions yielded N_S with a systematic error of $\sim 10\%$. The EPR spectra obtained for the a-Si samples studied in this paper are isotropic with a Landé g factor of 2.0055, typical of a-Si dangling bonds [42].

G. Doppler broadening spectroscopy

Positron annihilation experiments using DBS were performed to obtain the volume of empty space, or total volume

of nanovoids, as a function of sample depth. Amorphous silicon films were grown on c-Si substrates with the native oxide left intact on the substrate. In order to avoid attenuation from the native oxide on the *a*-Si surface, the films were etched in a buffered oxide etch (BOE) 10 : 1 solution for 10 min and then introduced into the measurement chamber and brought below 10^{-5} Torr within 25 min. After BOE the *S*-parameter values obtained from the surface of the *a*-Si films were >1.04 (see *S* definition below), typical of *a*-Si without native oxide. The vacuum pressure during typical measurements was less than 10^{-7} Torr. The positron incident beam energy was varied from 50 eV to 25 keV, which in c-Si yields implantation depths around 1 nm to 3 μm, respectively. In the present study, 25 keV yielded an implantation depth in the films' substrate; and data analysis is limited to below 40 keV to avoid systematic error from backscattered positrons that annihilate from the steel vacuum chamber walls.

A summary of DBS measurement and analysis procedures can be found elsewhere [43]. Photons emitted by positron annihilation were detected with a high-purity germanium detector from EG&G Ortec, with an energy resolution of 1.45-keV FWHM at the photon energy equivalent to the rest mass of positrons and electrons at 511 keV. To analyze Doppler broadening due to annihilations from nanovoids, we examined the photoelectric peak from 5×10^4 to 6×10^4 detected annihilations after suitable background subtraction. The accumulated events N_c in a narrow 1.45-keV window around the center and in the two wing regions N_w are compared with the total event number in the full photoelectric peak N_{tp}. The DBS parameters *S* and *W* are the ratios of N_c/N_{tp} and N_w/N_{tp}, respectively. The beam energy E in keV is converted to implantation depth d using the empirical formula d (nm) = $40 E^{1.6}/\rho$, where $\rho = 2.329$ g/cm^3 is the c-Si mass density [44]. VEPFIT software [45] is used to simulate the empty volume depth profiles optimizing *S*, layer thickness, and positron diffusion lengths, while layer density is set to that of c-Si. The *S* parameter yields information about the number of nanovoids and their size, from atomic vacancies to nanovoids [46]. The *W* parameter is sensitive to higher-momentum electrons and probes the elemental type of the nearest neighbor [47].

III. RESULTS

In this section we present the results for different properties as a function of growth temperature, growth rate, and thickness. We follow the same structure presented in Sec. II, showing first the results that provide insight into the structure and network, and later the structural defects: dangling bonds and nanovoids.

Topography, roughness and stress, atomic density, bond angle deviation, and local strain and nanovoid characterization were obtained from the same films, whereas other properties each required films grown on specific substrates. The errors reported in this paper reflect measurement uncertainty.

A. Topography, roughness, and stress

Figure 1 shows AFM images of samples grown at different temperatures and thicknesses. These images show the topography of the films' surface, where the roughness is con-
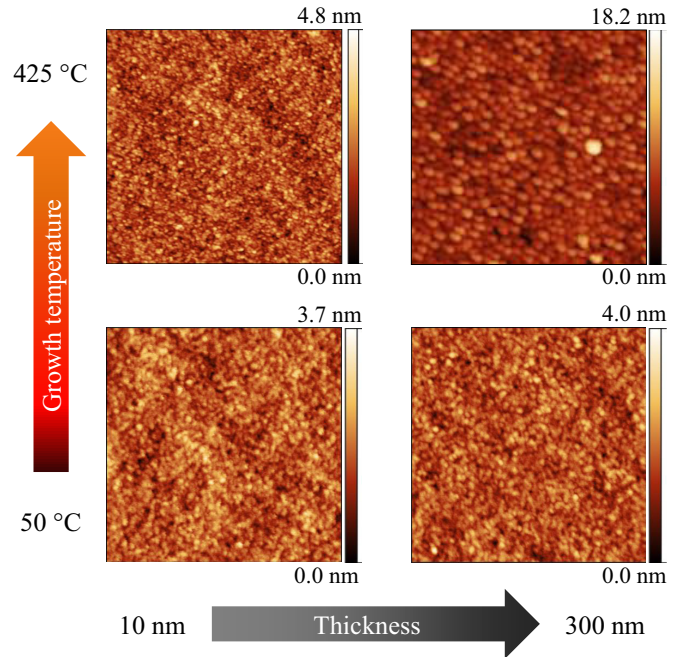

FIG. 1. AFM images of the surfaces of a subset of *a*-Si films: 10 and 300 nm thick, left and right, respectively, grown at 50 and 425 °C, bottom and top, respectively. The scale bars at the right side of each image show the absolute height variations for each film. All images are 1×1 μm^2.

siderably increased for thick films grown at high temperature. The statistical analysis of the images yields an average in-plane grain diameter of $\sim$12 nm for all films, except for the thick films grown at 425 °C that show grains of $\sim$20 nm. These grains measured by AFM are likely to be the end of amorphous columns observed previously in similar *a*-Si films [12].

The root-mean-square roughness Rq is shown in Fig. 2 as a function of thickness for films grown at 50, 225, and 425 °C. Rq is less than 0.5 nm, the same as the roughness
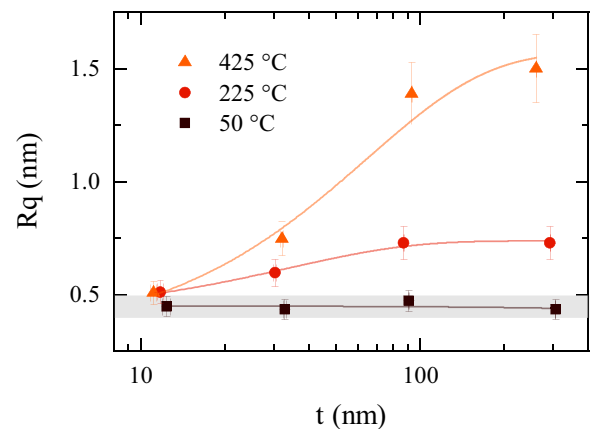

FIG. 2. rms roughness Rq of *a*-Si films as a function of thickness t for samples grown at 50 °C (brown squares), 225 °C (red circles), and 425 °C (orange triangles). All samples are grown at 0.5 Å/s. The gray area shows the substrate rms roughness. Curves are guides to the eye.
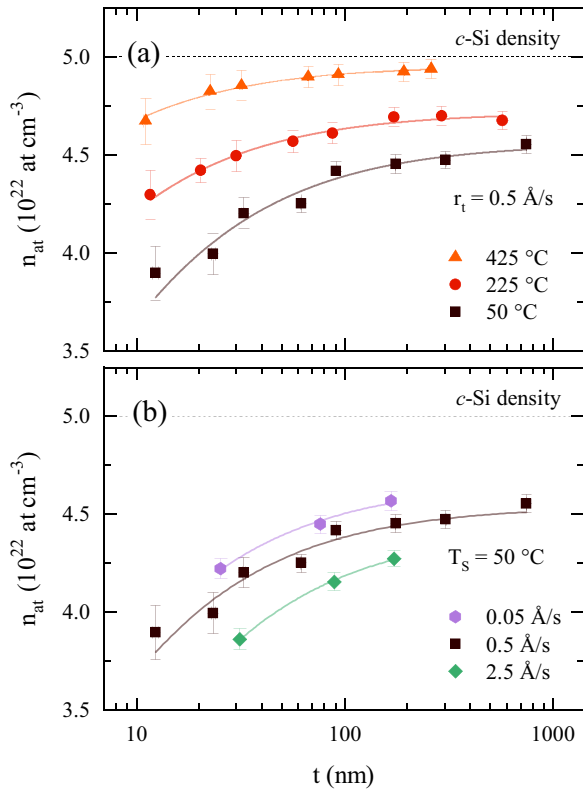
FIG. 3. Atomic density n_{at} of a-Si films as a function of thickness t for (a) growth temperatures of 50 °C (brown squares), 225 °C (red circles), and 425 °C (orange triangles) and (b) growth rates of 0.05 Å/s (lilac hexagons), 0.5 Å/s (brown squares), and 2.5 Å/s (green diamonds). In (a), all films are grown at 0.5 Å/s, and in (b), all films are grown at 50 °C. In both plots the c-Si density is given for reference (dashed horizontal line). Solid curves are guides to the eye.

of the substrate, for films grown at 50 °C at all thicknesses. At higher growth temperature, Rq increases proportionally to growth temperature and with thickness up to ∼100 nm, where it plateaus or slowly increases. A similar dependence of the surface roughness with thickness has been reported in hydrogenated a-Si films grown above room temperature [48,49].

The stress of a-Si films grown at room temperature was measured through the curvature of their substrates reporting tensile stresses of 694 ± 94 MPa for a 30-nm film, and 523 ± 20 MPa for a 90-nm film, which is comparable to other a-Si films grown by e-beam [50].

B. Atomic density

Atomic density n_{at} of a-Si films grown at different temperatures and rates was determined by RBS measurements in combination with profilometry, where the thicknesses were corrected after the AFM-measured roughness, as discussed in Sec. II B. The resulting data are shown in Fig. 3 as a function of thickness and show a remarkable and systematic dependence on thickness, growth temperature, and growth rate. Error bars are dominated by the thickness uncertainty (profilometry) for thin films and by areal atomic density uncertainty (RBS) for thick films. No observable discontinu-

ities are seen. The lowest-density films are quite underdense, ∼22% less than c-Si, whereas the highest-density films are ∼1% less dense than c-Si. Previous work on vapor-deposited a-Si films reported densities 19% smaller than that of c-Si [51], which was there suggested to be caused by low-density regions or nanovoids found in a-Si [52].

The atomic density of a-Si films grown by e-beam is thus highly dependent on thickness, growth temperature, and growth rate. We report density reductions with thickness for a-Si samples grown at room temperature between 25 and 10% for the thinnest and thickest films, respectively, when compared with c-Si density. Higher growth temperature and lower growth rate yield films with higher atomic density at any given thickness. Thick a-Si films, around 600 nm thick and grown at different temperatures, were subsequently annealed at 425 °C in UHV for 3 h. The film grown at 50 °C shows a thickness reduction from 598.6 to 593.1 nm (-5.5 ± 2.1 nm), which corresponds to a densification of ∼0.9%, whereas the thickness variation for films grown at 225 and 425 °C is within the error bars. Annealing at temperatures up to 425 °C thus does very little to the atomic density of a-Si films.

Atomic density provides a proxy to evaluate the thermodynamic and kinetic stability of amorphous solids [53], where it is known that stability can be tuned by means of growth temperature and rate on vapor-deposited glasses [54]. Increasing growth temperature increases surface mobility during deposition and allows atoms to reach lower-energy positions before being deposited over [55]. Similarly, slower growth rates allow these positions to be reached before mobile atoms are deposited over. In the particular case of a-Si and for the data presented in this paper, atomic density shows a stronger dependence on growth temperature and thickness than on growth rate. For this reason, we focus the present study on growth temperature and thickness dependence.

Resonant Rutherford backscattering spectrometry was performed to determine the oxygen content through the samples. The oxygen concentration of the a-Si films ranges between 0 and 3% and shows no correlation with thickness, growth temperature, or growth rate. Oxygen content did not increase with film aging (after 4 months). Neither contaminants nor water were observed via RBS and ERDA, respectively, in the films. Thickness measurements were also performed both immediately and 4 months after deposition; no changes were observed in thickness as a function of time.

C. Short- and medium-range order

In this section we present electron microscopy results, specifically diffraction, EELS, FEM, and high-resolution imaging results for ∼30-nm-thick a-Si samples grown at 0.5 Å/s, and at 50, 250, and 450 °C.

Figure 4 shows the average diffracted intensities $I(k)$. (k is defined as $k = \theta/\lambda$, where λ is the electron wavelength.) The peak positions are typical of a-Si and do not shift significantly from sample to sample. The first broad peak sits at 3.08 ± 0.05 nm^{-1}, which matches the c-Si $\langle 111 \rangle$ peak at 3.13 nm^{-1}. The second a-Si peak position at 5.54 ± 0.05 nm^{-1} sits between the c-Si reflections $\langle 220 \rangle$ at 5.2 nm^{-1} and $\langle 311 \rangle$ at 6.1 nm^{-1}. None of the data show the sharp peaks that would indicate nanocrystallization. Isolated nanocrystals were
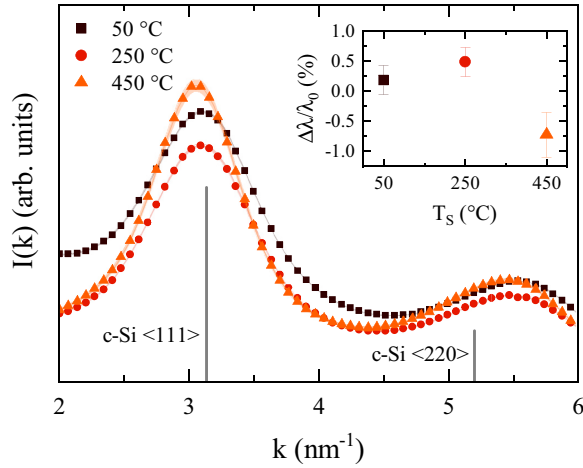
FIG. 4. Diffracted electron intensity $I(k)$ for a-Si thin films, ∼30 nm thick, grown at 0.5 Å/s, and at 50 °C (brown squares), 250 °C (red circles), and 450 °C (orange triangles). The diffraction peaks of c-Si are shown for reference. Shaded areas behind the data show their associated error. Inset: bulk plasmon relative change $\Delta\lambda/\lambda_0$ from EELS as a function of growth temperature T_S for the same samples.

FIG. 5. FEM data $V(k)$ as a function of wave vector k of a-Si thin films, ∼30 nm thick, grown at 0.5 Å/s, and at 50 °C (brown squares), 250 °C (red circles), and 450 °C (orange triangles). Shaded areas behind the data show their associated error. Gray stars show the MRO typically observed in a-Si films from Ref. [30]. The data for the 250 and 450 °C films, however, reveal a different MRO structure.

observed in the 450 °C film, indicating that under these growth conditions crystallization of a-Si starts at a temperature between 425 and 450 °C. Electron microscopy characterization was performed between the nanocrystals on fully amorphous regions. Differences in peak heights between films are not well quantified in these data. For more quantitatively accurate $I(k)$ and structure factor $S(q)$, synchrotron experiments are needed. Similarities between positions and widths for both low- and high-k peaks seen in Fig. 4, however, suggest that there are no significant differences in SRO for the films grown at different temperatures, consistent with previous work on a-Si [27].

EELS measurements performed on the same samples find an average bulk plasmon peak energy λ_0 of 16.6 eV. The relative change in λ_0, $\Delta\lambda/\lambda_0$, is +0.2, +0.5, and −0.7% for samples grown at 50, 250, and 450 °C, respectively (Fig. 4 inset). No significant change in average bond length between the films is observed. At constant composition and temperature, $\Delta\lambda/\lambda_0 \propto \sqrt{\Delta\rho/\rho_0}$, so the maximum change in density, not counting contributions from voids, is negligible. Together, these results show that the average bond length for atoms within the network is the same for the different samples. The SRO structure, specifically bond length and coordination, is independent of the growth conditions, and there is no change in atomic number density except what is created by introducing voids, to be discussed below.

FEM data of the same films shown in Fig. 4 are shown in Fig. 5. $V(k)$ peaks in amorphous materials typically occur at the same k as peaks in $I(k)$. That is the case for the film grown at 50 °C, but the films grown at 250 and 450 °C show a splitting of the first peak into a contribution near 3.1 nm⁻¹, common for all a-Si films, and another peak at lower k, closer to 2.6 nm⁻¹, which arises from some fraction of the atoms. This lower-k peak indicates that local structures exist in the higher-substrate-temperature samples with a larger
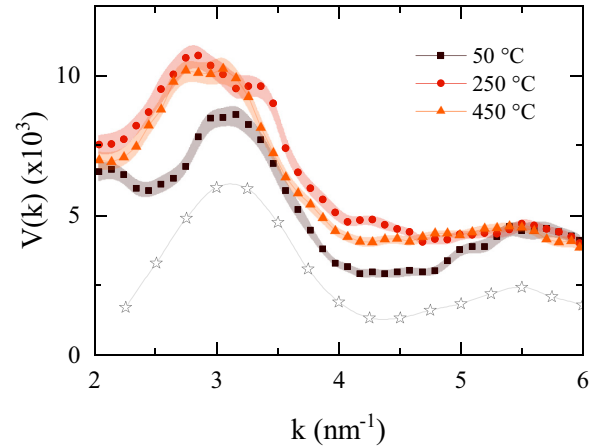
interatomic spacing than has been observed in previous FEM experiments on a-Si. There are no larger interatomic spacings in diamond structure Si, but a different crystal structure for Si, Si24, which has diffraction features at lower k corresponding to the peak position in $V(k)$ [56]. The low-k diffraction in Si24 arises from eight-membered rings. In Ref. [56], the Si24 crystal was synthesized at high pressure with Na atoms embedded in the crystal, filling the eight-atom Si rings. The material was brought to room pressure, and the Na atoms were removed using thermal degassing. The resulting crystal is stable at room temperature and atmospheric pressure. We do not suggest that there are nanocrystals of Si24 in the material, or even that we have created a paracrystalline analog to Si24. Instead we suggest that the low-k feature in $V(k)$ of these a-Si films grown at higher temperatures (225 and 425 °C) could be caused by structures in the amorphous network involving large rings of eight atoms or more, significantly larger than those typically present in a-Si [57]. These could even be viewed as extremely tiny nanovoids. However, we do not have a detailed structural model that quantitatively reproduces the FEM data, and alternatively the FEM data of the a-Si films grown at higher temperatures can also be explained as the diffraction signal from atoms on the surface of nanovoids.

Figure 6 shows underfocused, in-focus, and overfocused HRTEM images of the same samples. Under- and overfocused image pairs are a classical method for identifying voids in materials from the switch in contrast of the Fresnel fringe surrounding the void. The 50 °C sample shows clear evidence of columnar microstructure with nanometer-scale voids forming part of the column boundaries. The higher-temperature films do not have the columnar microstructure and do not have voids detectable by this method. In our previous work [12], cross-sectional TEM images (XTEM) of a-Si films show a columnar structure whose diameter increases with growth temperature. Such a structure is common in amorphous films grown by PVD techniques [58], including e-beam evaporation [59]. These images also reveal a region close to the substrate
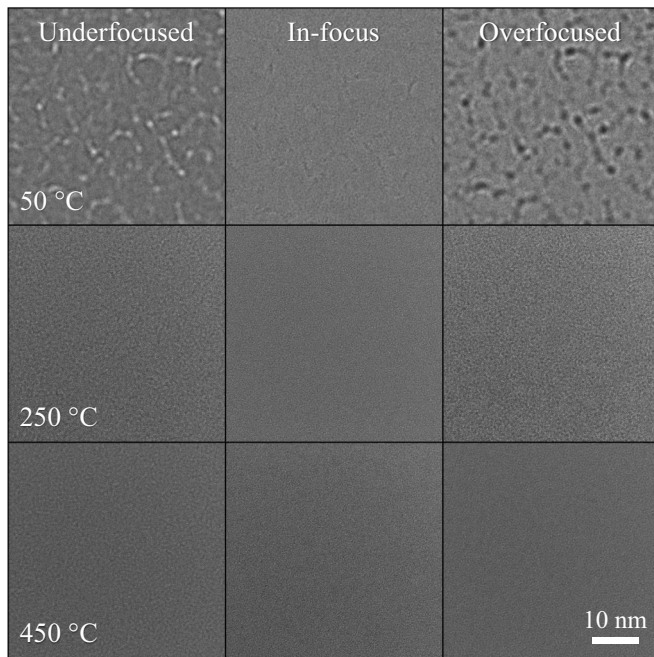
FIG. 6. HRTEM images of *a*-Si thin films ∼30 nm thick grown at 0.5 Å/s and at 50, 250, and 450 °C (top to bottom row, respectively). Columns from left to right show underfocused, in-focus, and overfocused images (see description in text). The film grown at 50 °C shows columnar structure, visible as wiggly lines, and voids, visible as white features in the underfocused image and black features in the same place in the overfocused image. Films grown at higher temperatures show no notable features.

FIG. 7. (a) Bond angle deviation $\Delta\theta$ and (b) trace of strain tr(ϵ) as a function of thickness t for samples grown at 50 °C (brown squares), 225 °C (red circles), and 425 °C (orange triangles). The right axis in both panels shows the measured quantity from which $\Delta\theta$ and tr(ϵ) are calculated as described in the text. Curves are guides to the eye.

interface that lacks columnar microstructure; this region is thicker for higher growth temperature. The columnar structure observed for the film grown at 50 °C has not developed yet for films grown at 250 and 450 °C; therefore the thickness at which columns develop in *a*-Si thin films is growth temperature dependent.

D. Bond angle deviation and local strain

Electron microscopy was used as described above to characterize SRO. $I(k)$ and $\Delta\lambda/\lambda_0$ are mostly sensitive to bond length and coordination number, and less to bond angles. We here turn to Raman spectroscopy to characterize the deviations from the tetrahedral angle θ that are found in *a*-Si. Figure 7(a) shows the bond angle deviation $\Delta\theta$ as a function of thickness for a series of growth temperatures. The range of $\Delta\theta$ found for these samples, approximately 9°–13°, is similar to values reported for *a*-Si model structures [34]. Films grown at 425 °C show $\Delta\theta$ that ranges from 9° to 10°. These values fall on the low end of those obtained from the radial distribution function of *a*-Si [6] and to our knowledge are amongst the lowest reported by experiment. Note that $\Delta\theta = 0°$ for c-Si and has been shown theoretically to be $\geqslant 6.6°$ for *a*-Si [34], evidence that the transition from crystalline to amorphous structures is not continuous. $\Delta\theta$ is considered a measure of disorder at very short length scales: nearest-neighbor distances, or around 2 Å. At each thickness, $\Delta\theta$ is lower for films grown at higher tem-
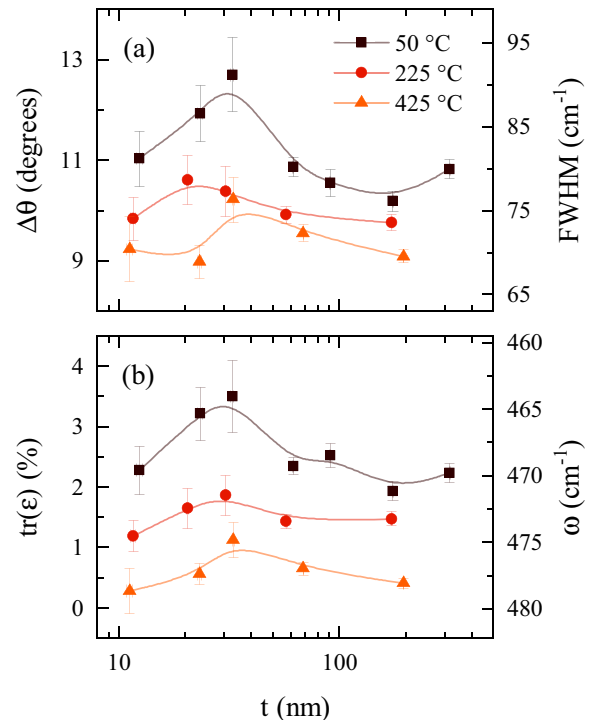
peratures, indicating that disorder decreases with increasing growth temperature.

Figure 7(b) shows the trace of the local strain tr(ϵ) calculated from ω as described in Sec. II D. $\Delta\theta$ and tr(ϵ) shown in Figs. 7(a) and 7(b), respectively, are correlated. Higher growth temperature thus yields less disordered and less strained films at all thicknesses. However, the monotonic trend observed for atomic density as a function of thickness is not seen for these properties: Both $\Delta\theta$ and tr(ϵ) increase with thickness up to a maximum value and then decrease. This behavior is most clear in films grown at 50 °C, where the maximum values of $\Delta\theta$ and tr(ϵ) occur near 30 nm. For films grown at higher temperature, the peak in $\Delta\theta$ and tr(ϵ) is more subtle and may occur at different thicknesses.

Raman data analysis shows a relaxation process in which disorder and local strain reduce above a *critical thickness*; however, it is unclear whether this process implies a structural change in the atoms underneath, i.e., the *reorganization* of the atoms already deposited.

Following the procedure described in Sec. II, we study n_{at} and $\Delta\theta$ of several *a*-Si etched films. In Fig. 8 we compare these results to equivalent as-deposited films to probe for reorganization during growth. The larger error bars are due to increased surface roughness and thickness uncertainty after the etch process. All films etched and measured were grown at 50 °C because they exhibit the largest change in atomic density and bond angle deviation as a function of thickness, as seen in Figs. 3(a) and 7(a), respectively. The gray areas
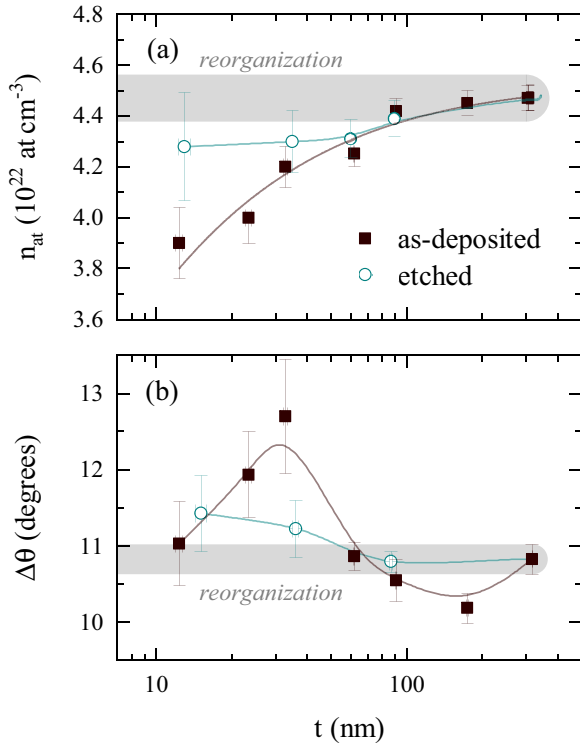
FIG. 8. (a) Atomic density n_{at} and (b) bond angle deviation $\Delta\theta$ as a function of thickness t for as-deposited (brown closed squares) and etched (cyan open circles) films. All films were grown at 50 °C and 0.5 Å/s; etched films initially were ∼300 nm thick. Gray areas labeled "reorganization" show the extrapolated n_{at} and $\Delta\theta$ values of the ∼300 nm as-deposited films prior to the etch process (see text for further details). Curves are guides to the eye.

labeled "reorganization" in Fig. 8 are the extrapolated n_{at} and $\Delta\theta$ values of thick as-deposited films. A complete reorganization would yield etched thin films with the higher n_{at} and lower $\Delta\theta$ of the as-deposited thicker films, whereas a lack of reorganization would yield etched thin films with the lower density and higher disorder of the as-deposited thin films.

Figure 8(a) shows that atomic density n_{at} from etched films is higher than that of as-deposited films with similar thickness, most consistent with reorganization, with etched films lying within the error bars of the as-deposited values of thick films and well above the values of as-deposited thin films. Bond angle deviation $\Delta\theta$ from etched films is lower than that of as-deposited films with similar thickness, shown in Fig. 8(b), which suggests a reduction of disorder, and is also most consistent with reorganization of the early layers of atoms deposited near the substrate.

It has been proposed that due to the large interface energy between substrate and film, thin films prepared by physical-vapor deposition grow via a Volmer-Weber mode [60,61]. This proposed growth mode is in agreement with stress measurements in e-beam evaporated a-Si films, which show the nucleation of columns that correlate with the transition from compressive to tensile stress regimes as a function of thickness [50].

The results presented in this section show structural relaxation as a function of thickness that leads to the reduction
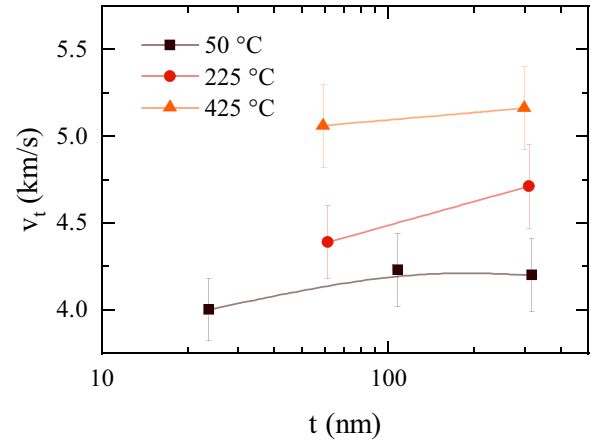

FIG. 9. Transverse sound velocity v_t as a function of thickness t of a-Si films grown at 50 °C (brown squares), 225 °C (red circles), and 425 °C (orange triangles). Curves are guides to the eye.

of disorder and local strain, compatible with the previously described studies of the stress evolution during growth of evaporated a-Si [50]. From Ref. [50], we also see that the dependence with thickness of the compressive-to-tensile stress transition is in agreement with our structural observations by XTEM, which show the onset of the columnar growth [12].

E. Transverse sound velocity

Transverse sound velocity v_t as a function of thickness for films grown at different temperatures is shown in Fig. 9. The sound velocity is only weakly dependent on thickness, perhaps within the error bars of a constant, whereas it increases with increasing growth temperature.

The sound velocity in solids, including amorphous solids, is due to phonons that propagate through the material, with a velocity that is independent of the frequency of the phonons for relatively long wavelength phonons. The sound velocity is generally dependent on the interatomic spacing, the atomic mass, and the interatomic bond strength. In a-Si, the increase in sound velocity v_t with increasing growth temperature, shown in Fig. 9, correlates with the reduction of atomic disorder ($\Delta\theta$) and local strain [tr(ϵ)], shown in Figs. 7(a) and 7(b), respectively. That sound velocity depends strongly on growth temperature, but is not strongly dependent on thickness at constant growth temperature, despite significant changes in atomic density with thickness, shows that sound waves are carried through an a-Si network. Sound velocity therefore is not affected directly by the overall density, i.e., it is not much affected by nanovoids.

F. Dangling bond density

Dangling bond density ρ_{DB} has long been considered a defect metric and is correlated with surface-state transitions in silicon [62]. In photovoltaic and semiconductor technologies, a-Si is prepared with hydrogen in order to passivate dangling bonds and create high-quality, or device-quality, films. The dangling bond densities of our films are on the order of 10^{18} spins/cm³ (see Fig. 10). Standard a-Si has dangling bond densities of ∼10^{19} spins/cm³, and device-quality a-Si:H
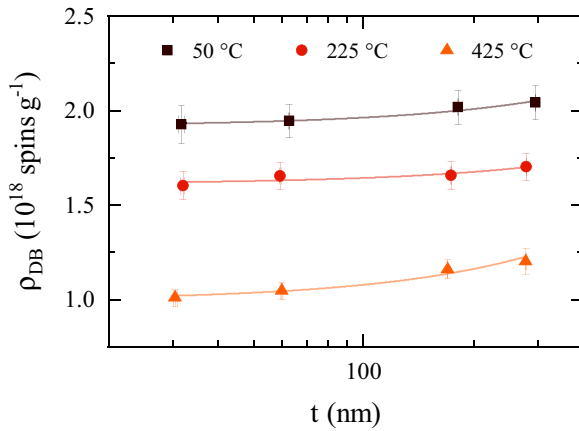
FIG. 10. Dangling bond density ρ_{DB} as a function of thickness t of a-Si films grown at 50 °C (brown squares), 225 °C (red circles), and 425 °C (orange triangles). All samples were grown at 0.5 Å/s. Curves are linear fits to the data.

FIG. 11. S parameter normalized to the c-Si S parameter ($S_{c\text{-}Si} = 0.5324$) as a function of incident positron energy E of three a-Si films grown at 50 °C and 0.5 Å/s, with thicknesses of 66, 183, and 308 nm (light, medium, and dark gray, respectively). Data at 0 keV are values from the a-Si surface and move progressively through the film for increasing energies until the beam reaches the substrate at $\sim$30 keV. Inset: detail at low energies showing the accuracy of the single (dashed curves) and dual (solid curves) models. The dual model improves its relative accuracy with respect to the experimental data almost 50% compared with the single model. Curves have been vertically shifted to better show the fittings.

shows values of $<10^{16}$ spins/cm³ [63]. We report ρ_{DB} per unit mass (g⁻¹) rather than per unit volume (cm⁻³) because the atomic density of our samples is not constant, which makes the former a more accurate metric for direct comparisons.

Figure 10 shows that ρ_{DB} decreases significantly with increasing growth temperature, and mildly increases with thickness for all growth temperatures. The former statement is consistent with the strong dependence of atomic density n_{at} on growth temperature, but is the opposite to how n_{at} depends on thickness, suggesting that the relationship between n_{at} and ρ_{DB} is not simple. The dependence of ρ_{DB} on growth temperature suggests that the nucleation of dangling bonds is inversely proportional to surface diffusion, specifically, that higher growth temperature yields more fourfold coordinated atoms. That dangling bond density mildly *increases* with thickness for all growth temperatures suggests that the formation of this type of defect is not related to the mechanisms responsible for the films' atomic density or the atomic reorganization process previously discussed.

The short- and medium-range order, bond angle deviation, local strain, and dangling bond density results report information about the distribution of silicon atoms in the films and about specific electronic defects; specifically, EELS results show that the interatomic distances do not change with growth temperature. Therefore these results do not explain the very low atomic density values, and particularly that of the thinnest films grown at room temperature. In the next section, we study the presence of nanovoids, which in a-Si cannot be detected by microscopy techniques, but are considered a common structural defect in a-Si [64].

G. Nanovoid characterization

Doppler broadening spectroscopy results for films of different thicknesses and grown at 50 °C are shown in Fig. 11, where the S parameter is plotted as a function of energy. Energy is proportional to penetration depth (as described in Sec. II G), and for the films reported in this paper, it ranges from 0 keV (surface) to $\sim$30 keV (substrate) for the thickest films. We could not measure films thinner than 60 nm
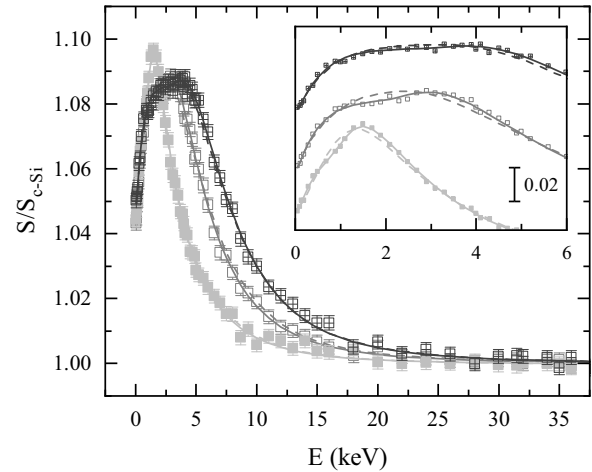
due to lack of sensitivity. In this paper, the data acquired from the annihilation of positrons indicate that all a-Si films measured, grown at different temperatures and for different thicknesses, contain nanovoids. Specifically, the normalized S-parameter $S/S_{c\text{-}Si}$ values are associated with nanovoids with at least five missing atoms ($n = 5$) [46]. The correspondence between $S/S_{c\text{-}Si}$ and n is established for nanovoids with $n < 6$ [65], whereas the size of larger nanovoids is extrapolated from the previous correspondence and should be taken with caution [46]. Electron microscopy cannot detect the presence of nanovoids in a-Si films due to the atomic superposition and the low atomic scattering factor of silicon. For these reasons, we can only provide a lower bound for nanovoids with more than six missing atoms.

We used two different models to simulate the experimental data [66]: (1) a *single* volume of empty space that is uniformly distributed throughout the film, and (2) *dual* volumes of empty space that are uniformly distributed throughout the film, in which the nanovoid volume closer to the substrate is different from that closer to the surface. The simulations yield better results for the dual model, which is almost 50% more accurate than the single model (see inset in Fig. 11). The dual volume of empty space is the simplest model to probe whether the data suggest a more complex distribution of nanovoids than a single-volume-of-empty-space model. These results suggest that at least two different distributions of nanovoids are present on a-Si films thicker than 60 nm, with the interface between the two distributions at 31 ± 6 nm from the substrate for films grown at 50 °C, and at 59 ± 17 nm for films grown at 425 °C. This increase in the first nanovoid layer thickness with growth temperature is in agreement with the thickness
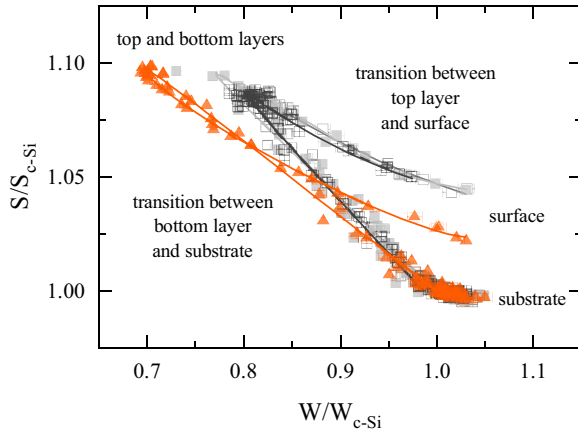
FIG. 12. *S* vs *W* plots for films grown at 50 °C, with 66, 183, and 308 nm (light, medium, and dark gray squares, respectively), and for a film grown at 425 °C with 291 nm (orange triangles). Vertical and horizontal axes are normalized to the c-Si *S* and *W* values, with $S_{c-Si} = 0.5324$ and $W_{c-Si} = 0.0237$. Solid curves are *S-W* fits considering a bilayer distribution of nanovoids. Labels indicate the position where positrons annihilate from film surface to substrate.

dependence of void track formation with growth temperature seen in *a*-Si films grown by Floro *et al.* [50]. The dual model also reports that the first layer, closer to the substrate, has a larger volume of empty space than the second layer, closer to the surface. Specifically, for the first and second layers we obtain >25 and 6 missing atoms for films grown at 50 °C and >19 and 5 missing atoms for films grown at 425 °C, respectively.

S vs *W* plots are shown in Fig. 12 for the same films shown in Fig. 11 and a ~300-nm film grown at 425 °C. Typical *S* vs *W* plots show annihilated positrons with a constant *S*-to-*W* ratio from surface to substrate (a single straight line). Our results, however, show a V-shaped line due to the presence of different types of nanovoids across the film (nanovoids of different size). In other words, different *S-W* pairs, or slopes, represent nanovoids with a chemically distinct surface bonding. Steeper *S-W* slopes correspond to larger nanovoids. Points at the end of the "V" with moderate *S* and high *W* values exist at the surface of the film and progressively change by following the "V" shape to its vertex with low *S* and high *W*, where positrons annihilate at the interface between the two distributions of nanovoids (see Fig. 12 and corresponding labels). The chemical change of the nanovoids across the distinct distributions is due to the distinct chemical nature of electrons present in them, i.e., to the nanovoid sizes and not to their concentration.

The analysis of the *S* data suggests that a single distribution is less likely than a dual distribution of empty space volume, or total nanovoid volume, as shown in the inset of Fig. 11, and the *S-W* data in Fig. 12 show more than one type of nanovoid, which significantly differ in the nature of the bonding at their inner surfaces. Films grown at all temperatures show that the distribution closer to the surface has a smaller empty space volume than the distribution closer to the substrate. Additionally, the empty space volume in the distribution closer to the

surface is smaller for films grown at 425 °C compared with films grown at 50 °C.

In *a*-Si, dangling bonds are found to occur on the inner surfaces of nanovoids [67–70]. However, the relationship in the literature between dangling bonds and nanovoids is unclear.

The existence of nanovoids in *a*-Si, confirmed by DBS measurements, provides an explanation for the the low atomic density values of the films reported in this paper.

IV. DISCUSSION AND CONCLUSIONS

The atomic density n_{at} of *a*-Si films increases with increasing growth temperature and thickness, and with reducing growth rate (Fig. 3). In all cases, films are underdense, with n_{at} as high as ~99% of c-Si density for films grown at 425 °C and thicker than 300 nm, and as low as ~78% of c-Si density, which is achieved for the thinner films grown at room temperature. FEM results on ~30-nm-thick films show significant differences in MRO, as shown in Fig. 5, despite no change in SRO (Fig. 4), which suggests that larger membered rings appear as the growth temperature increases. Measurements of the plasmon peak energy relative change $\Delta\lambda/\lambda_0$, presented in the inset of Fig. 4, show no significant changes in atomic density between films as a function of growth temperature. Therefore the reduction of n_{at} can only be attributed to voids. Those voids must be of nanometer scale, as large voids would be visible in HRTEM.

Raman data analysis reveals a reduction of the atomic disorder, the bond angle deviation $\Delta\theta$, with increasing growth temperature [Fig. 7(a)]. This dependence on growth temperature is also observed for the local strain tr(ϵ) of the *a*-Si films [Fig. 7(b)]. These data show a nonmonotonic behavior of disorder and local strain with thickness, particularly for films grown at room temperature, whose magnitudes build up and then reduce to their initial values. The characterization of nanovoids shows that the best simulations of the data (Fig. 11) and the analysis of the *S-W* plots (Fig. 12) suggest the presence of at least two different types, or sizes, of nanovoids, with larger empty space volume near the substrate. The thickness at which the transition between the two distributions occurs, increasing from approximately 30 to 60 nm with increasing growth temperature, coincides with the critical thickness seen by Raman spectroscopy. The stress results also report higher tensile stress for thinner films, ~30 nm thick, than for thicker films, ~90 nm thick. We therefore speculate that at the critical thickness a structural relaxation process occurs, triggering the formation of columns observed by electron microscopy [12,50], and the reduction of $\Delta\theta$ (atomic disorder) and tr(ϵ) (local strain). Floro *et al.* [50] saw similar effects, albeit at slightly different thicknesses.

The study of n_{at} and $\Delta\theta$ from etched samples [Figs. 8(a) and 8(b), respectively] shows reorganization of the films' structure during growth. These results do not suggest a direct relationship between reorganization and critical thickness, even though they might be caused by a common underlying relaxation process that takes place during growth. We note that the atomic density increases monotonically with thickness, suggesting that the reorganization of the films continuously happens during growth, whereas the critical thickness seems to be triggered by a specific event. Additionally, DBS results

based on a dual distribution of empty space volume show that the total volume of nanovoids is reduced as films grow thicker. Our data do not allow us to establish whether reorganization and critical thickness are two processes independent of each other, or whether one is triggered by the other.

Dangling bond density ρ_{DB} results report up to $\sim$1 defect in 10^4 atoms, which implies that Si atoms in a-Si films are largely fully coordinated despite their notably low atomic densities in some films, with up to $\sim$22% missing atoms (compared with c-Si). These results suggest that only a very small fraction (less than 1%) of nanovoids contain even one dangling bond. Additionally, energetic considerations suggest that having two dangling bonds in a single nanovoid is unlikely because two nearby undercoordinated silicon atoms will bond together. Therefore the increase in ρ_{DB} with thickness (Fig. 10) suggests an increase in the nanovoid number, which in combination with the densification of the films (Fig. 3) implies that nanovoids become smaller as films grow thicker. This conclusion is also supported by the DBS results (Fig. 12).

Two distinct processes happen in e-beam evaporated a-Si films during growth: (i) The first process is a sudden structural relaxation at a *critical thickness*, which depends on growth temperature and correlates with the formation of columns [12,50] (Fig. 6). This process is also captured by the reduction of atomic disorder and local strain (Fig. 7) and by the reduction of the nanovoids' size and their total volume (Fig. 12). (ii) The second process is a continuous *reorganization* of the atoms seen in the atomic density and bond angle deviation of etched thicker films (Fig. 8). This process is responsible for the reduction of the total volume of nanovoids as films grow thicker, which leads to the continuous densification of the films (Fig. 3) and to the reduction of TLSs [10,71].

As we previously reported, the TLS density of a-Si obtained from films equivalent to those presented in this paper depends strongly on growth conditions, with a dependence that can be completely explained by plotting TLS density as a function of atomic density. Remarkably, and as previously observed [10], the excess heat capacity at low temperature, below 10 K, of thinner a-Si films (112 nm) is larger than that of thicker films (278 nm). This observation cannot solely be explained by the larger concentration of nanovoids in the first layer (near the substrate), which indeed would yield thinner films with larger excess specific heat, but not heat capacity.

This excess heat capacity reduction can only be explained by atomic reorganization, which effectively reduces the number of TLSs when films grow thicker. Similarly, the mechanical loss of thinner a-Si films (59 nm) is larger than that of thicker films (299 nm) [71]. Our data suggest that the structural origin of TLSs in a-Si likely occurs in highly disordered regions where nanovoids are present. The reduction of atomic disorder and nanovoid volume (increase in atomic density) correlates with the reduction of TLSs observed in thicker a-Si films. The reorganization of the atoms as films grow thicker plays a crucial role in reducing TLSs in a-Si, and it is likely to be related to local structural rearrangements caused by structural relaxation processes. The reduction of TLSs with growth temperature is likely to be related to surface diffusion mechanisms during growth, since surface diffusion is enhanced by temperature. Additionally, Fig. 9 shows that sound velocity increases with increasing growth temperature, while its dependence on thickness is within the error bars of no dependence, suggesting that the sound velocity depends on properties of the a-Si network, such as bond angle disorder, and not on the presence of nanovoids; meanwhile, nanovoids and their environment, and not the constrained network, are responsible for the mechanisms that enable TLSs in a-Si.

[1] *Technology and Applications of Amorphous Silicon*, 1st ed., edited by R. A. Street, Springer Series in Materials Science Vol. 37 (Springer, Berlin, 2000).

[2] N.-M. Park, C.-J. Choi, T.-Y. Seong, and S.-J. Park, Phys. Rev. Lett. **86**, 1355 (2001).

[3] W. D. Oliver and P. B. Welander, MRS Bull. **38**, 816 (2013).

[4] R. X. Adhikari, K. Arai, A. F. Brooks, C. Wipf, O. Aguiar, P. Altin, B. Barr, L. Barsotti, R. Bassiri, A. Bell, G. Billingsley, R. Birney, D. Blair, E. Bonilla, J. Briggs, D. D. Brown, R. Byer, H. Cao, M. Constancio, S. Cooper *et al.*, Classical Quantum Gravity **37**, 165003 (2020).

[5] J. Steinlechner and I. W. Martin, Phys. Rev. D **103**, 042001 (2021).

[6] J. Fortner and J. S. Lannin, Phys. Rev. B **39**, 5527 (1989).

[7] K. Laaziri, S. Kycia, S. Roorda, M. Chicoine, J. L. Robertson, J. Wang, and S. C. Moss, Phys. Rev. Lett. **82**, 3460 (1999).

[8] W. A. Phillips, J. Low Temp. Phys. **7**, 351 (1972).

[9] B. L. Zink, R. Pietri, and F. Hellman, Phys. Rev. Lett. **96**, 055902 (2006).

[10] D. R. Queen, X. Liu, J. Karel, T. H. Metcalf, and F. Hellman, Phys. Rev. Lett. **110**, 135901 (2013).

[11] X. Liu, D. R. Queen, T. H. Metcalf, J. E. Karel, and F. Hellman, Phys. Rev. Lett. **113**, 025503 (2014).

[12] D. R. Queen, X. Liu, J. Karel, H. C. Jacks, T. H. Metcalf, and F. Hellman, J. Non-Cryst. Solids **426**, 19 (2015).

[13] W. A. Phillips, Rep. Prog. Phys. **50**, 1657 (1987).

[14] J. M. Martinis, K. B. Cooper, R. McDermott, M. Steffen, M. Ansmann, K. D. Osborn, K. Cicak, S. Oh, D. P. Pappas, R. W. Simmonds, and C. C. Yu, Phys. Rev. Lett. **95**, 210503 (2005).

[15] J. Gao, J. Zmuidzinas, B. A. Mazin, H. G. Leduc, and P. K. Day, Appl. Phys. Lett. **90**, 2013 (2007).

[16] R. W. Simmonds, M. S. Allman, F. Altomare, K. Cicak, K. D. Osborn, J. A. Park, M. Sillanpää, A. Sirois, J. A. Strong, and J. D. Whittaker, Quantum Inf. Process. **8**, 117 (2009).

[17] J. Steinlechner, I. W. Martin, A. S. Bell, J. Hough, M. Fletcher, P. G. Murray, R. Robie, S. Rowan, and R. Schnabel, Phys. Rev. Lett. **120**, 263602 (2018).

[18] R. Birney, J. Steinlechner, Z. Tornasi, S. MacFoy, D. Vine, A. S. Bell, D. Gibson, J. Hough, S. Rowan, P. Sortais, S. Sproules, S. Tait, I. W. Martin, and S. Reid, Phys. Rev. Lett. **121**, 191101 (2018).

[19] J. L. Pitters, L. Livadaru, M. B. Haider, and R. A. Wolkow, J. Chem. Phys. **134**, 064712 (2011).

[20] M. Morita, T. Ohmi, E. Hasegawa, M. Kawakami, and M. Ohwada, J. Appl. Phys. (Melville, NY) **68**, 1272 (1990).

[21] D. Misra, W. Zhong, R. A. Bartynski, V. Patel, and B. Singh, Semicond. Sci. Technol. **11**, 816 (1996).

[22] M. J. Madou, *Fundamentals of Microfabrication: The Science of Miniaturization*, 2nd ed. (CRC Press, Boca Raton, FL, 2002), Chap. 4, pp. 214–215.

[23] G. G. Stoney, Proc. R. Soc. London, Ser. A **82**, 172 (1909).

[24] C. A. Klein, J. Appl. Phys. (Melville, NY) **88**, 5487 (2000).

[25] M. Mayer, in *The Fifteenth International Conference on the Application of Accelerators in Research and Industry*, AIP Conference Proceedings Vol. 475 (AIP, Melville, NY, 1999), pp. 541–544.

[26] P. M. Voyles, J. M. Gibson, and M. M. J. Treacy, J. Electron Microsc. **49**, 259 (2000).

[27] P. Voyles and D. Muller, Ultramicroscopy **93**, 147 (2002).

[28] J. Hwang, Z. H. Melgarejo, Y. E. Kalay, I. Kalay, M. J. Kramer, D. S. Stone, and P. M. Voyles, Phys. Rev. Lett. **108**, 195505 (2012).

[29] Y. Zhang, E. C. Glor, M. Li, T. Liu, K. Wahid, W. Zhang, R. A. Riggleman, and Z. Fakhraai, J. Chem. Phys. **145**, 114502 (2016).

[30] P. M. Voyles and J. R. Abelson, Sol. Energy Mater. Sol. Cells **78**, 85 (2003).

[31] N. Zotov, M. Marinov, N. Mousseau, and G. Barkema, J. Phys.: Condens. Matter **11**, 9647 (1999).

[32] M. Mecklenburg, W. A. Hubbard, E. R. White, R. Dhall, S. B. Cronin, S. Aloni, and B. C. Regan, Science **347**, 629 (2015).

[33] P. Palanisamy and J. M. Howe, J. Appl. Phys. (Melville, NY) **110**, 024908 (2011).

[34] D. Beeman, R. Tsu, and M. F. Thorpe, Phys. Rev. B **32**, 874 (1985).

[35] M. Marinov and N. Zotov, Phys. Rev. B **55**, 2938 (1997).

[36] R. L. C. Vink, G. T. Barkema, and W. F. van der Weg, Phys. Rev. B **63**, 115210 (2001).

[37] I. D. Wolf, Semicond. Sci. Technol. **11**, 139 (1996).

[38] E. Bonera, M. Fanciulli, and D. N. Batchelder, J. Appl. Phys. (Melville, NY) **94**, 2729 (2003).

[39] D. A. Strubbe, E. C. Johlin, T. R. Kirkpatrick, T. Buonassisi, and J. C. Grossman, Phys. Rev. B **92**, 241202(R) (2015).

[40] B. E. White and R. O. Pohl, in *Thin Films: Stresses and Mechanical Properties V*, MRS Symposium Proceedings Vol. 356 (Materials Research Society, Pittsburgh, PA, 1994), p. 567.

[41] X. Liu and R. O. Pohl, Phys. Rev. B **58**, 9067 (1998).

[42] P. A. Thomas, M. H. Brodsky, D. Kaplan, and D. Lepine, Phys. Rev. B **18**, 3059 (1978).

[43] F. Tuomisto and I. Makkonen, Rev. Mod. Phys. **85**, 1583 (2013).

[44] P. J. Schultz and K. G. Lynn, Rev. Mod. Phys. **60**, 701 (1988).

[45] A. van Veen, H. Schut, M. Clement, J. M. M. de Nijs, A. Kruseman, and M. R. IJpma, Appl. Surf. Sci. **85**, 216 (1995).

[46] P. G. Coleman, J. Phys.: Conf. Ser. **265**, 012001 (2011).

[47] M. Clement, J. M. M. De Nijs, P. Balk, H. Schut, and A. Van Veen, J. Appl. Phys. (Melville, NY) **79**, 9029 (1996).

[48] R. Brüggemann, P. Reinig, and M. Hölling, Thin Solid Films **427**, 358 (2003).

[49] A. H. M. Smets, W. M. M. Kessels, and M. C. M. van de Sanden, Appl. Phys. Lett. **82**, 865 (2003).

[50] J. A. Floro, P. G. Kotula, S. C. Seel, and D. J. Srolovitz, Phys. Rev. Lett. **91**, 096101 (2003).

[51] R. C. Chittick, J. Non-Cryst. Solids **3**, 255 (1970).

[52] S. C. Moss and J. F. Graczyk, Phys. Rev. Lett. **23**, 1167 (1969).

[53] M. D. Ediger, J. Chem. Phys. **147**, 210901 (2017).

[54] L. Berthier, P. Charbonneau, E. Flenner, and F. Zamponi, Phys. Rev. Lett. **119**, 188002 (2017).

[55] Z. Shi, P. G. Debenedetti, and F. H. Stillinger, J. Chem. Phys. **134**, 114524 (2011).

[56] D. Y. Kim, S. Stefanoski, O. O. Kurakevych, and T. A. Strobel, Nat. Mater. **14**, 169 (2015).

[57] D. Beeman and R. Alben, Adv. Phys. **26**, 339 (1977).

[58] G. S. Bales and A. Zangwill, J. Vac. Sci. Technol. A **9**, 145 (1991).

[59] U. v. Hulsen, P. Thiyagarajan, and U. Geyer, in *Thin Films: Structure and Morphology*, MRS Symposium Proceedings Vol. 441 (Materials Research Society, Pittsburgh, PA, 1997), p. 391.

[60] J. A. Floro, S. J. Hearne, J. A. Hunter, P. Kotula, E. Chason, S. C. Seel, and C. V. Thompson, J. Appl. Phys. (Melville, NY) **89**, 4886 (2001).

[61] J. A. Floro, E. Chason, R. C. Cammarata, and D. J. Srolovitz, MRS Bull. **27**, 19 (2002).

[62] J. E. Rowe and H. Ibach, Phys. Rev. Lett. **31**, 102 (1973).

[63] A. Mahan, B. Nelson, S. Salamon, and R. Crandall, J. Non-Cryst. Solids **137-138**, 657 (1991).

[64] E. Guerrero and D. A. Strubbe, Phys. Rev. Materials **4**, 025601 (2020).

[65] M. Hakala, M. J. Puska, and R. M. Nieminen, Phys. Rev. B **57**, 7621 (1998).

[66] W. Shi, M. Theelen, A. Illiberi, N. Barreau, S. J. van der Sar, M. Butterling, H. Schut, W. Egger, M. Dickmann, C. Hugenschmidt, M. Zeman, E. Brück, and S. W. H. Eijt, Phys. Rev. Materials **2**, 105403 (2018).

[67] G. A. N. Connell and J. R. Pawlik, Phys. Rev. B **13**, 787 (1976).

[68] J. C. Knights, G. Lucovsky, and R. J. Nemanich, J. Non-Cryst. Solids **32**, 393 (1979).

[69] R. A. Street and D. K. Biegelsen, Solid State Commun. **33**, 1159 (1980).

[70] J. Dąbrowski, H. J. Müssig, and G. Wolff, Phys. Rev. Lett. **73**, 1660 (1994).

[71] M. Molina-Ruiz, Y. J. Rosen, H. C. Jacks, M. R. Abernathy, T. H. Metcalf, X. Liu, J. L. DuBois, and F. Hellman, Phys. Rev. Materials **5**, 035601 (2021).